Numerical modeling of FRP strips bonded to a masonry substrate

Numerical modeling of FRP strips bonded to a masonry substrate

Antonio Maria D'Altri[1*], Christian Carloni[1], Stefano de Miranda[1], Giovanni Castellazzi[1]

Department of Civil, Chemical, Environmental, and Materials Engineering (DICAM), University of Bologna, Viale del Risorgimento 2, 40136 Bologna, Italy

Abstract

In this paper, the debonding phenomenon in FRP-strengthened masonry is numerically investigated. A 3D finite element model is developed to reproduce an experimental set-up of single-lap shear tests. Brick and mortar are modeled separately by two plastic-damage constitutive laws. Perfect adhesion between the FRP strip and masonry is assumed. Firstly, the numerical model is used to simulate experimental tests. A good agreement between the experimental and numerical results in terms of load-slip response is observed. Then, further finite element analyses are carried out to gain an insight on the effects of (i) the thickness and mechanical properties of the mortar joints and (ii) the width of the FRP strip on the debonding phenomenon.

Keywords: Masonry, FRP, Debonding, FE analysis, DIC

1. Introduction

Externally bonded fiber-reinforced polymer (FRP) composites are a well-established strengthening technique to increase the in-plane [1-9] and out-of-plane capacity [10-13] of existing masonry structures. The ability of FRPs to increase the load-carrying capacity of the structural element to which they are applied is tied to their bond behavior. Debonding of the FRP from masonry is a brittle phenomenon, which typically occurs prior to exploiting the full tensile capacity of the composite. Debonding failure often implies fracturing of the quasi-brittle substrate, which results in a thin layer of the substrate left attached to the composite.

As one of the most important aspects of the FRP technology, debonding has been studied copiously over the last two decades. The majority of the studies published in the area of FRP-masonry bond behavior deals with small-scale direct-shear tests [14-28]. The experimental evidence has pointed out that the periodic presence of mortar joints [16, 17, 23, 24, 29-34] within the masonry pattern entails for a variable (periodically) transferable load at the

*corresponding author: antoniomaria.daltri2@unibo.it

FRP-masonry interface. The maximum transferable load at the interface could be equal to, greater than, or less than the maximum transferable load at the FRP-brick interface depending on the geometry of masonry, the interfacial properties (i.e. the mechanical and physical properties of brick and mortar), and the stiffness of the composite.

The effect of the mortar joints on the transferable load at the FRP-masonry interface has been investigated numerically and analytically by means of different approaches. If the FRP-masonry interface is modelled as a zero-thickness material and a fracture mechanics Mode-II loading condition is assumed, a cohesive material law (CML) can be defined for the FRP-brick and FRP-mortar interfaces [16]. The CML is defined in terms of the interfacial shear stress and slip between the FRP and the substrate. Within this approach, Carloni and Focacci [34] has provided a closed-form expression of the transferable load at the FRP-masonry interface that depends on the CMLs of FRP-brick and FRP-mortar interfaces. Similarly, the same approach was used to study the role of mortar joints by means of a one-dimensional finite element (FE) model [17], two-dimensional FE model [35, 36], or three-dimensional FE model [37, 38].

Numerically, a different approach can be pursued, which assumes perfect bond between the FRP strip and the substrate. Debonding is then associated with a damage or fracture process within the substrate. Along this line, Fedele and Milani [39, 40] studied the entire stress field within the masonry bulk. A similar approach was used in [41], where the effect of the characteristics of the mortar and the FRP axial stiffness on the load response was highlighted.

In this paper, the debonding phenomenon in FRP-strengthened masonry is investigated by means of a numerical campaign. A 3D finite element model of a single-lap shear test is set up. The constraints of the single-lap shear test are accounted for by appropriate boundary conditions. Perfect adhesion between FRP and masonry is assumed. Clay brick and mortar are modeled by means of two different plastic-damage laws.

Firstly, numerical results are discussed and compared with a set of experimental data. In particular, the periodic response of the transferable load at the FRP-masonry interface due to the effect of mortar joints is numerically investigated. Then, further FE analyses are carried out to shed light on the effects of the thickness and mechanical properties of the mortar joints, and the width of the FRP strip on the debonding phenomenon.

The paper is organized as follows. In Section 2, the experimental campaign is briefly described. The numerical set-up and the mechanical model adopted for brick and mortar are described in Section 3. Section 4 presents the comparison between numerical and ex-

perimental results. Finally, further numerical investigation of open issues of the debonding phenomenon are presented and discussed in Section 5.

2. Experimental tests

In this section a brief recall of the experimental work published in [16, 17] is provided to set the basis of the numerical study presented herein, which is built upon the experimental evidence. Direct single-lap shear tests were conducted by Carloni ad Subramaniam [16, 17]. The push-pull configuration was employed. Masonry blocks were restrained in between a steel plate and the base of the testing machine by means of 4 steel bars, while the FRP strip was pulled. The test was controlled by increasing at a constant rate the relative displacement between the FRP and the masonry substrate at the beginning of the bonded area, which was named global slip and was determined as the average of the reading of two linear variable differential transformers (LVDT). The test set-up is shown in Figure 1. Additional details of the set-up can be found in [16, 17]. It should be noted that additional data and set-ups of single-shear tests are available in the literature, see for example [18, 21, 22, 24, 27, 29, 30, 31, 54]. The typical experimental load response of the FRP-masonry joint is shown in Figure 2 (green line), which corresponds to specimen DS_MS_1 reported in [17]. Digital image correlation (DIC) was used for all specimens in order to obtain the strain field on the surface of the specimen. For all specimens, failure was associated with debonding at the FRP-substrate interface. A thin layer of substrate remained attached to the composite strip. Prior to performing direct shear tests, compressive strengths and Young's moduli of brick and mortar were determined. The averages strengths resulted equal to 35.6 MPa and 9.8 MPa, respectively; while the averages moduli resulted equal to 30700 MPa and 16850 MPa, respectively.

From the experimental campaign used as reference in this paper [16, 17], some important features that have been highlighted when discussing the role of mortar joints on the load-carrying capacity of the FRP-strengthened masonry include:

- Load drops in single-lap shear tests are associated with the presence of mortar joints;
- The effect of mortar joints, in terms of load drop, is more emphasized when the length of the stress transfer zone at the FRP-brick interface is smaller than the length of the brick. If the length of the stress-transfer zone is greater than the size of the brick, the maximum load-carrying capacity of the FRP-brick interface cannot be reach;

- The extent of the load drop is slightly affected by the properties of the mortar inter-face. Even a drastic decrease in fracture energy of the FRP-mortar interface implies a relatively marginal decrease of the load drop;
- The load drop is also influenced by the length of the mortar joints;
- The load drop occurs when the mortar joint is involved in load transfer. As the load-carrying capacity of the FRP-mortar interface is lower than that of the brick, a decrease of the transferable load at the FRP-masonry interface with respect to the FRP-brick interface is associated with the portion of the stress transfer zone corresponding to the mortar joint.

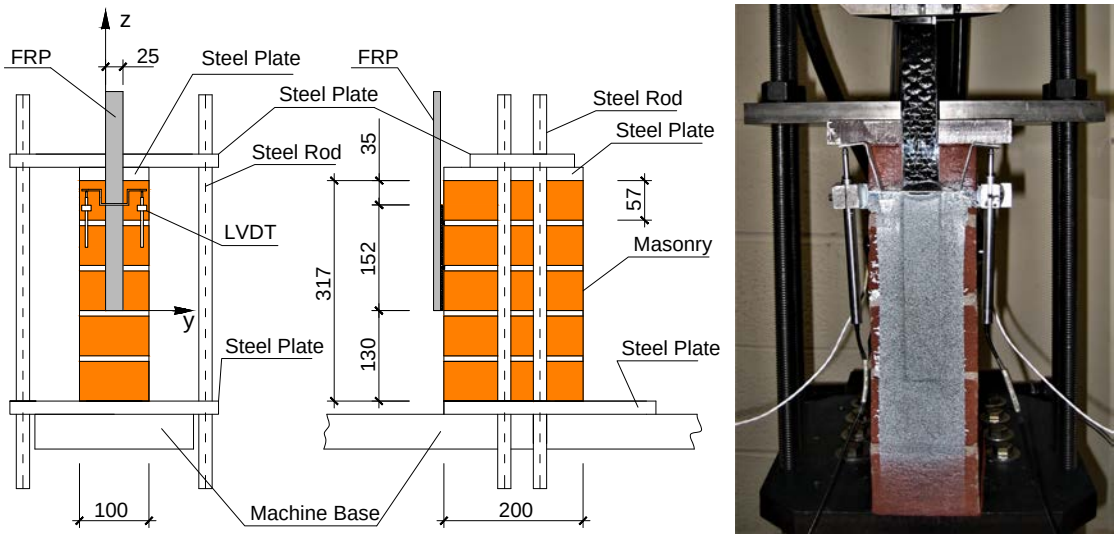

(a) (b)

Figure 1: (a) Sketch of the experimental setup; (b) Photo of specimen DS_MS_1 [17].

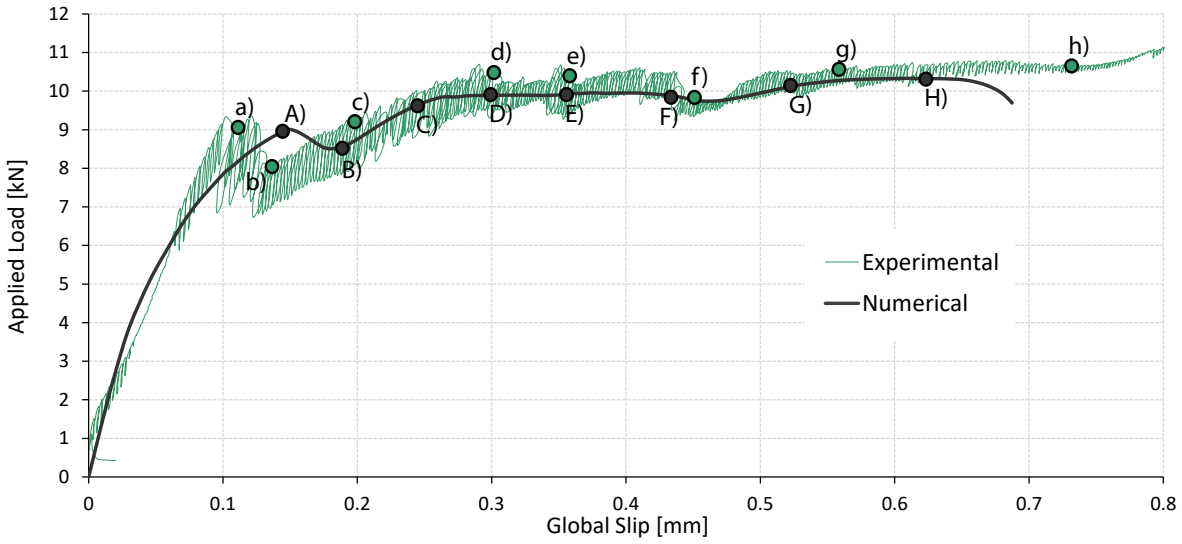

Figure 2: Applied load-global slip curves of specimen DS_MS_1 [17]: comparison between experimental and numerical results.

3. Numerical modeling

In this section, the 3D finite element model used to simulate the single-lap shear test, presented in the previous section, is described. Bricks and mortar joints are modeled separately by two plastic-damage constitutive laws. Perfect adeshion between the FRP strip and the masonry substrate is considered. Debonding in FRP-strengthened masonry usually occurs within a thin layer of the substrate [43, 44], i.e. a thin layer of brick and mortar remains attached to the FRP strip. Conversely, the failure at the actual FRP-masonry interface without any substrate attached is not a typical failure mode. Therefore, the assumption of perfect adhesion between FRP and masonry appears suitable as fracture in the thin layer is achieve through damage of the elements.

3.1. Numerical set-up

Brick and mortar have been modeled with 8-nodes hexahedral elements, whereas the FRP strip has been modeled with 4-nodes membrane elements (i.e. plane elements without out-of-plane stiffness), see Figure 3. This choice had a twofold purpose: (i) to guarantee a good compatibility in between 8-nodes and 4-nodes elements (i.e. they share the same nodes and they are characterized by the same nodal unknowns); and (ii) to neglect automatically the out-of-plane stiffness of the FRP strip (which appears a reasonable hypothesis for the set-up studied). The mesh adopted is depicted in Figure 3(a). It counts 20,844 nodes and 18,576 finite elements, out of which 18,104 are hexahedral elements. Due to the symmetry of the setup, only half of the specimen has been modeled.

Boundary conditions have been selected to match the experimental set-up constraints (Figure 3(b)). In particular, a layer of linear elastic hexahedral elements (brown elements in Figure 3) has been considered at the loaded end of the masonry block in order to account for the deformability of the steel rods used as constraint in [16]. Additionally, the deformable layer, coupled with the boundary conditions sketched in Figure 3(b), allows the masonry block to rotate about the axis r (Figure 3(b)), which is a common experimental outcome [16].

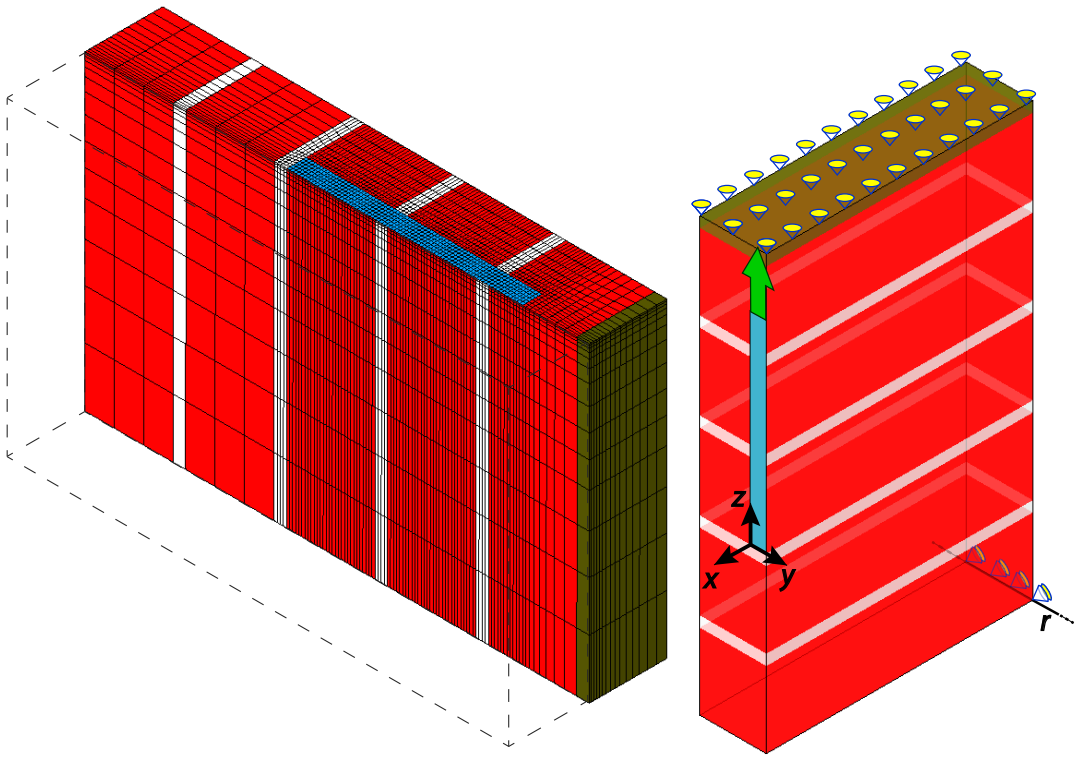

(a) (b)

Figure 3: Numerical set-up: (a) mesh and (b) boundary conditions.

3.2. Mechanical model for brick and mortar

Plastic-damage nonlinear behavior for brick and mortar both in tension and compression is supposed. Isotropic material behavior based on the plastic-damage model developed by Lee and Fenves [45] and implemented in the software package Abaqus Standard [46] has been considered. The constitutive model is briefly described below to present the main parameters involved in the numerical model.

Isotropic degradation damage is assumed and, if a scalar degradation damage variable $0 \leq D < 1$ is used to represent the isotropic damage and the concepts of strain decomposition and effective stress are employed, then the Cauchy stress tensor $\boldsymbol{\sigma}$ becomes:

$$\boldsymbol{\sigma} = (1 - D)\bar{\boldsymbol{\sigma}} = (1 - D)\boldsymbol{E}_0(\boldsymbol{\varepsilon} - \boldsymbol{\varepsilon}^p), \tag{1}$$

where $\bar{\boldsymbol{\sigma}}$ is the effective stress tensor, $\boldsymbol{E}_0$ is the initial undamaged elastic stiffness tensor, $\boldsymbol{\varepsilon}$ is the strain tensor and $\boldsymbol{\varepsilon}^p$ is the plastic part of the strain tensor.

Uniaxial tensile f_t and compressive f_c strength functions are expressed in terms of two independent hardening variables k_t and k_c:

$$f_t(k_t) = [1 - d_t(k_t)]\bar{f}_t(k_t), \;\; f_c(k_c) = [1 - d_c(k_c)]\bar{f}_c(k_c), \tag{2}$$

where $0 \leq d_t < 1$ and $0 \leq d_c < 1$ are the tensile and compressive scalar damage variables, respectively, and $\bar{f}_t(k_t)$ and $\bar{f}_c(k_c)$ represent the uniaxial tensile and compressive strengths, respectively, in the effective-stress responses. The single degradation damage variable in (1) is used to describe both tensile and compressive degradation responses:

$$D = 1 - (1 - d_t)(1 - d_c). \tag{3}$$

It should be noted that D in (3) satisfies the condition $0 \leq D < 1$ and is equal to either d_t when $d_c = 0$ (uniaxial tensile case) or d_c when $d_t = 0$ (uniaxial compressive case). Accordingly, the tensile and compressive uniaxial strength functions (2) can be written, respectively, as:

$$f_t = (1 - D)\bar{f}_t, \;\; f_c = (1 - D)\bar{f}_c. \tag{4}$$

The plastic strain rate $\dot{\boldsymbol{\varepsilon}}^p$ is assumed to be generated from a scalar plastic potential function Φ. Nonassociative flow rule is considered to control dilatancy and a Drucker-Prager type function is adopted as plastic potential, which, in terms of effective stresses, has the

form:

$$\Phi(\bar{\boldsymbol{\sigma}}) = \sqrt{(\epsilon f_{t0} \tan\psi)^2 + 3J_2(\bar{\boldsymbol{\sigma}})} + \frac{1}{3} I_1(\bar{\boldsymbol{\sigma}}) \tan\psi, \tag{5}$$

where I_1 is the first invariant of the stress tensor, J_2 is the second invariant of the stress deviator, f_{t0} is the initial uniaxial tensile strength, ϵ is a smoothing parameter generally assumed equal to 0.1 [47], and ψ is the dilatancy angle of the quasi-brittle material. ψ is typically assumed equal to 10 degrees in agreement with experimental evidences available in the literature for low compressive states [48] and previous numerical models recently adopted in different case studies [47, 49, 50].

If vector $\boldsymbol{k} = [k_t, k_c]^T$ is introduced, the plastic-damage model employs the yield surface $F(\bar{\boldsymbol{\sigma}}, \boldsymbol{k})$ proposed in [51] and further developed in [45], which has the following form in the effective-stress space:

$$F(\bar{\boldsymbol{\sigma}}, \boldsymbol{k}) = \frac{1}{1-\alpha}[\alpha I_1(\bar{\boldsymbol{\sigma}}) + \sqrt{3J_2(\bar{\boldsymbol{\sigma}})} + \beta(\boldsymbol{k})\langle\bar{\sigma}_{\max}\rangle - \gamma\langle-\bar{\sigma}_{\max}\rangle] + \bar{f}_c(k_c) = 0, \tag{6}$$

where $\bar{\sigma}_{\max}$ is the algebraically maximum principal stress in the effective-stress space, α and γ are dimensionless constants and $\beta(\boldsymbol{k})$ is a function of the hardening variables. α depends on the ratio f_{b0}/f_{c0} between the biaxial initial compressive strength f_{b0} and the uniaxial initial compressive strength f_{c0} through the relationship $\alpha = [(f_{b0}/f_{c0}) - 1]/[2(f_{b0}/f_{c0}) - 1]$. Typically, $f_{b0}/f_{c0} = 1.16$, which implies $\alpha = 0.12$ [51]. γ appears only in triaxial compression and is defined as $\gamma = 3(1-\rho)/(2\rho-1)$, where ρ is a constant that represents the ratio of the second stress invariant on the tensile meridian to that on the compressive meridian at initial yielding. A typical value of $\rho = 2/3$ leads to $\gamma = 3$ [51]. Finally, $\beta(\boldsymbol{k})$ is assumed to be a function of the hardening variables through the relationship $\beta(\boldsymbol{k}) = -[\bar{f}_c(k_c)]/[\bar{f}_t(k_t)](1-\alpha) - (1+\alpha)$. The adopted yield surface is depicted in the deviatoric plane reported in Figure 4. The model parameters used in numerical analyses presented in the next sections are reported in Table 1.

Figure 5 shows the curves adopted for the uniaxial behavior in compression and in tension and the evolution of the scalar damage variables. The scalar damage variable evolution with respect to the axial strain has been assumed substantially proportional to the decay of the uniaxial stresses, both in compression and in tension, as commonly adopted to model masonry material [38, 52]. Furthermore, uniaxial curves are in agreement with the materials mechanical characterization [16] and the stress-strain uniaxial relationship obtained in [53] and with typical values of fracture energy [53]. It should be pointed out that for the tensile behavior, no direct experimental information was available. Therefore, the tensile uniaxial

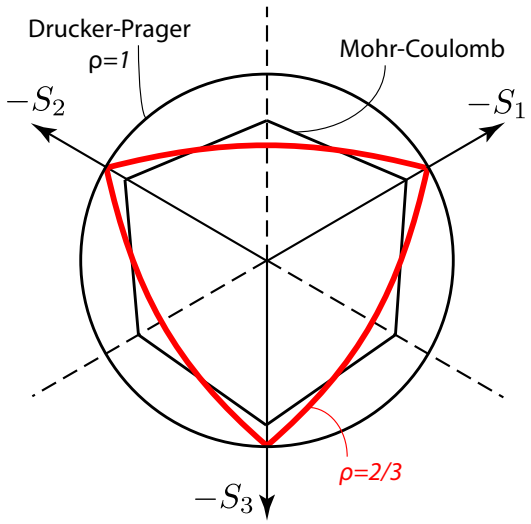

Figure 4: Yield surface in the deviatoric plane.

behavior of brick and mortar has been assumed based on other studies in the literature (see for example [38]), i.e. the tensile strength was assumed equal to one fifth and one forth of the compressive strength [38] for mortar and brick, respectively. As it can be noted, after the softening branch (both in compression and in tension) the curves are characterized by a constant residual stress that ranges between 3% and 5% of the uniaxial strength. This assumption, as well as the limitation of the scalar damage variables at 0.96 (instead of 1, which is the maximum value that they can theoretically reach), have been used to avoid possible numerical drawbacks.

Mesh objectivity in the softening branch passes through an indirect definition of the fracture energy, i.e. the model is local, and regularization requires scaling of the fracture energies by means of the equivalent length $l_{eq} = \alpha_h \sqrt{V_e} = \alpha_h (\sum_{\rho=1}^{n_\rho} \sum_{\xi=1}^{n_\xi} \sum_{\eta=1}^{n_\eta} detJ w_\rho w_\xi w_\eta)$ where w_ρ,w_ξ and w_η are the weight factors of the Gaussian integration scheme, J the Jacobian of the transformation, V_e the element area, and α_h a modification factor that depends on the typology of the finite element used. In this way, the mesh size does not significantly influence the material response.

Table 1: Model parameters and material properties used in the numerical analyses.

Model parameters	Values	Reference
ρ	2/3	[51]
f_{b0}/f_{c0}	1.16	[51]
ψ	10 degrees	[48, 47]
ϵ	0.1	[47]
Mortar Young's modulus [MPa]	16850	[16]
Mortar Poisson's ratio	0.19	[38]
Brick Young's modulus [MPa]	30700	[16]
Brick Poisson's ratio	0.24	[38]

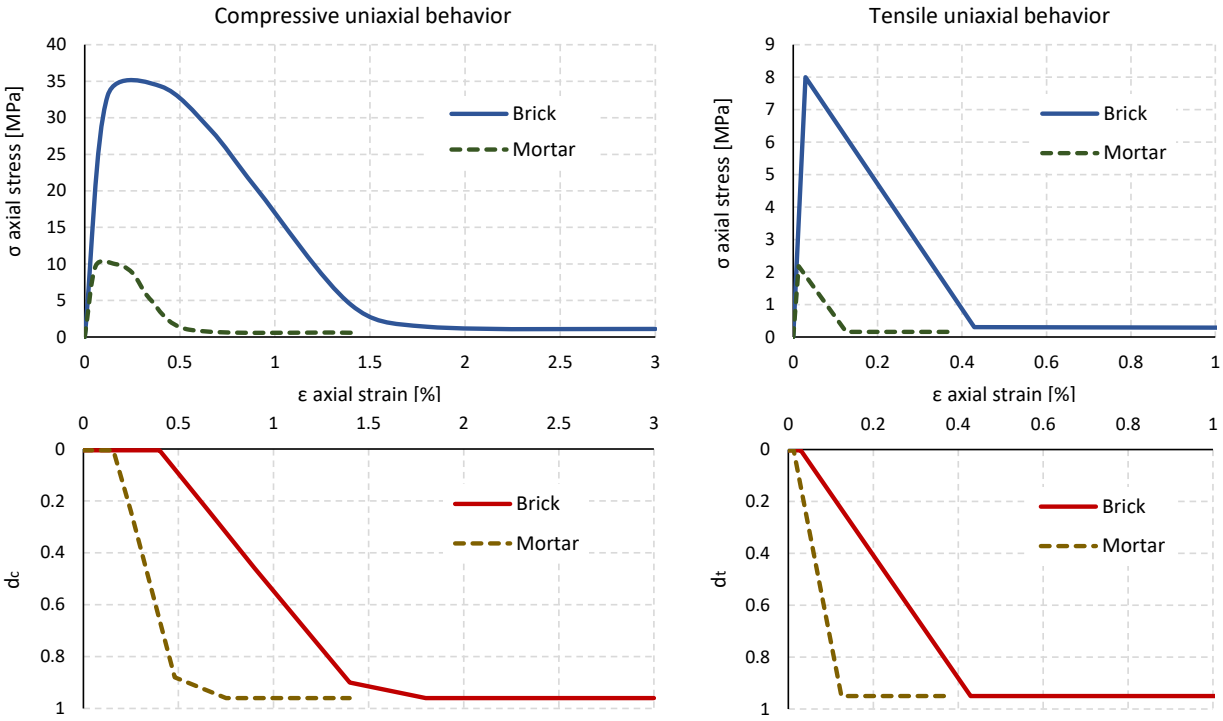

Figure 5: Curves for uniaxial behavior in compression and tension and damage variables for brick and mortar.

4. Comparison between experimental and numerical results

In order to evaluate the effectiveness of the modeling approach adopted, a comparison between numerical and experimental results has been carried out in terms of applied load-global slip curves (Figure 2) and strain contour plots referred to the FRP strip (Figure 6).

As it can be noted in Figure 2, the numerical and experimental curves are in good agreement. In particular, the numerical simulation adequately predicts the two load drops, due to the change in interfacial properties between brick and mortar, the trend of the experimental response, as well as the value of the load at which it levels off. In fact, although the first numerical peak load occurs at a slip greater than the experimental one, its magnitude is very close to the experimental load. Furthermore, the numerical model adequately predicts the magnitude of two post-peak plateaus, as highlighted in Figure 2. Therefore, the numerical approach adopted appears satisfactorily accurate to investigate the debonding phenomenon in FRP-strengthened masonry.

Figure 6 provides a comparison of the development of the longitudinal component of the strain on the strip surface (ε_{zz} based on the reference system shown in Figure 3) obtained experimentally (by means of DIC) and numerically. The points marked in Figure 2 have been considered to plot the contour maps in Figure 6. Such points have been selected on the two curves to represent key points with the same mechanical meaning, e.g. first peak of the curve, first drop of the curve, etc. Due to the presence of glue used to mount the LVDTs, which alters the strain distribution in the last part of the bonded area of the specimens, the comparison of the contour plots has been carried out for $z < 145$ mm. By comparing the experimental and numerical contour plots (Figure 6), a good agreement on the magnitude of the strain component as well as of the deformation process can be observed. This outcome further show the reliability of the numerical approach adopted.

Figures 7, 8, and 9 illustrate the evolution of the compressive and tensile scalar damage variables as well as the shear stress distribution throughout the single-lap shear test, respectively. For the sake of clarity, the FRP strip was not shown in the figures. Points marked in Figure 2 have been considered to plot the contour plots of Figures 7, 8, and 9.

It is worth noting that most of the damaged finite elements (both compressive, Figure 7, and tensile, Figure 8) belong to the first layer of elements (1 mm thick) beneath the FRP strip. A different trend occurs for the tensile scalar damage variable in the mortar joints. Indeed, its values appear greater than zero in some elements through the depth of the joints, as shown in Figure 8, which suggests that, throughout the test, adjacent bricks

tend to rotate one with respect to another and open near the FRP strip.

Figure 9 provides an insight into the process of the stress transfer between the FRP strip and the masonry substrate. Figure 9 shows that the magnitude of the stress transferred over the mortar joints is considerably lower than the stress transferred through the brick substrate, due to the different mechanical (interfacial) properties between brick and mortar. Mortar joints represent a sort of interruption of the stress transfer along the FRP-masonry interface. This phenomenon can be related to the load drops observed in Figure 2.

The damage model utilized in the simulations is characterized by two independent damage scalar variables in tension and compression. Therefore, by excluding the compressive damage in the simulations, shear stresses are still transferred in the zones which experience tensile damage and, hence, the overall response (in terms of force-slip curves) tends to be characterized by a significant hardening and the shear stress distribution is considerably different from the one depicted in 9 (i.e. characterized by a widespread shear stress distribution also in the zone where tensile damage occurred. Thereby, the adoption of compressive damage appears fundamental to catch the main features of the debonding phenomenon in the framework of a two-damage-variables-based plastic-damage constitutive law.

Finally, it has to be pointed out that in single-lap shear tests some researchers observed the formation of inclined cracks in the substrate and, also, the detaching of wedges. In-deed, in [54] the failure in concrete or clay brick after debonding in shear bond tests was characterized by very small inclined cracks, whose inclination is significantly smaller than 45 degrees, indicating that the failure mode is not related with a pure shear state. Further-more, the detachment of wedges at the free end of the strip has been recorded in several studies, depending on the application of a plaster layer before the FRP reinforcement [54], the type of the material used in the substrate [24] and the set-up used in the tests [40]. The outcomes of the experimental campaign [16] used as reference in this paper showed that the debonding process, which started from the loaded end of the FRP strip, was characterized by the detachment of a very thin layer (1-2 mm) of the masonry substrate without a clear formation of inclined cracks and, also, without a clear detachment of wedges at the free end of the strip. This phenomenon was in good agreement with the numerical results obtained.

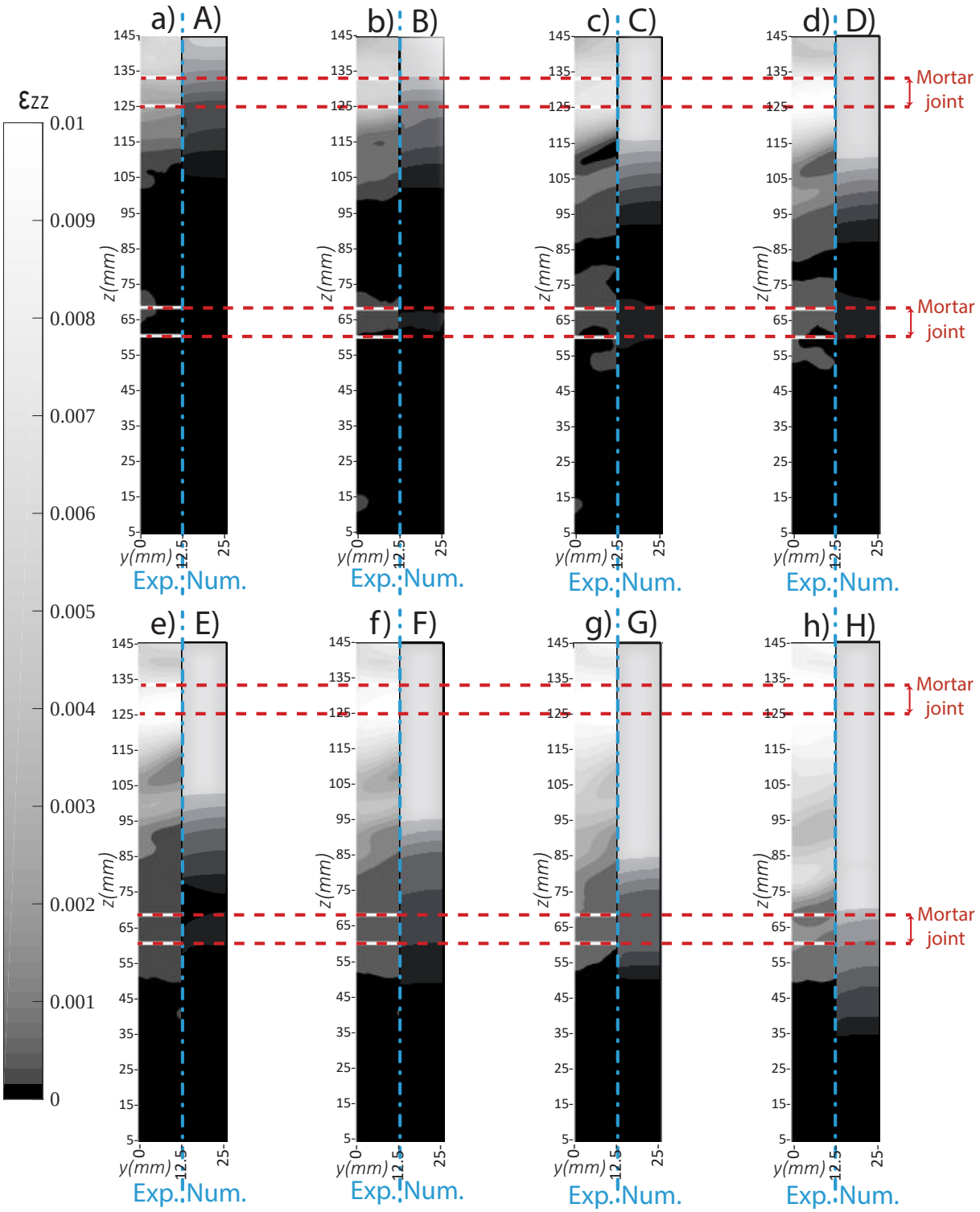

Figure 6: Comparison of strain contour plots of the FRP strip.

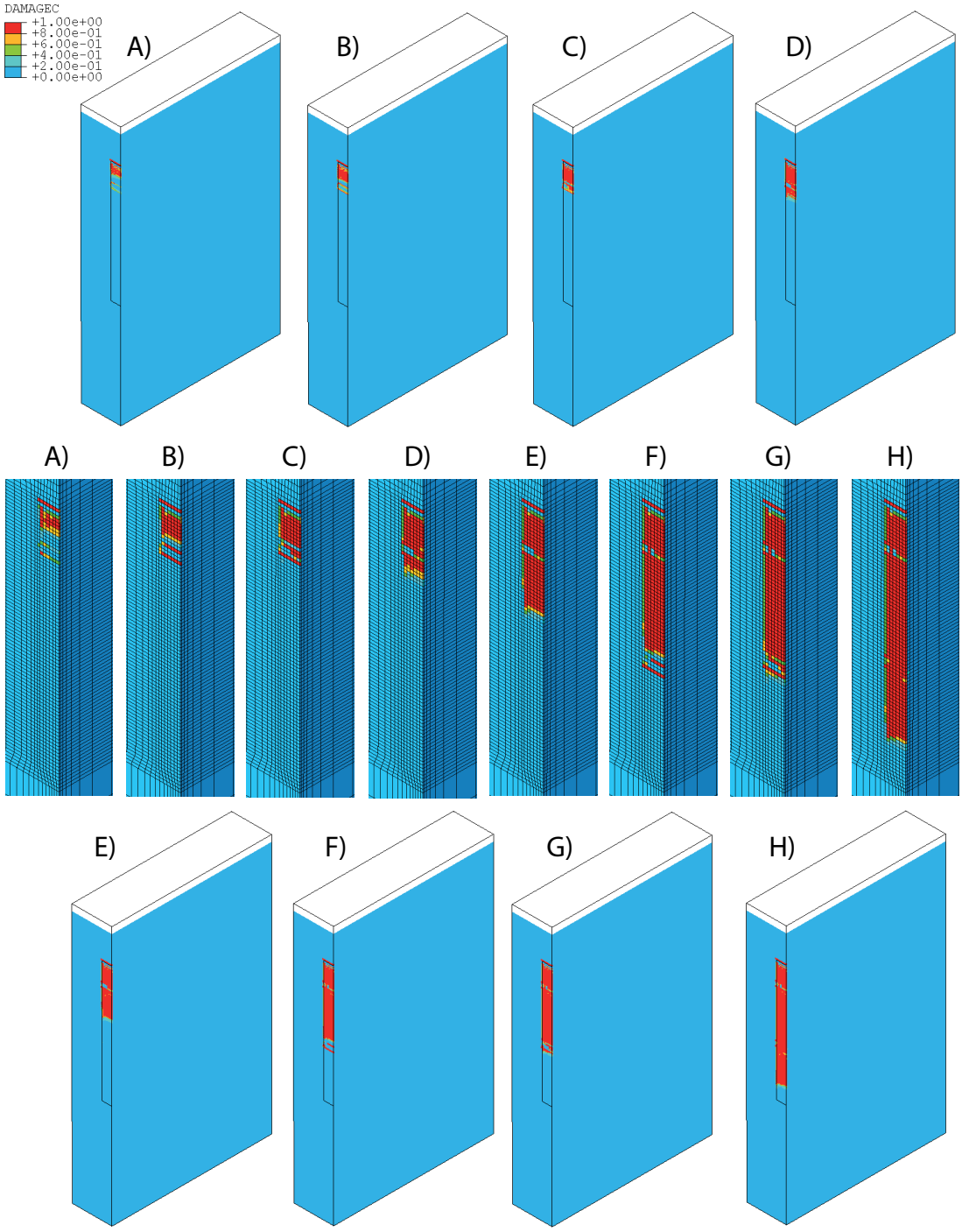

Figure 7: Compressive damage contour plots.

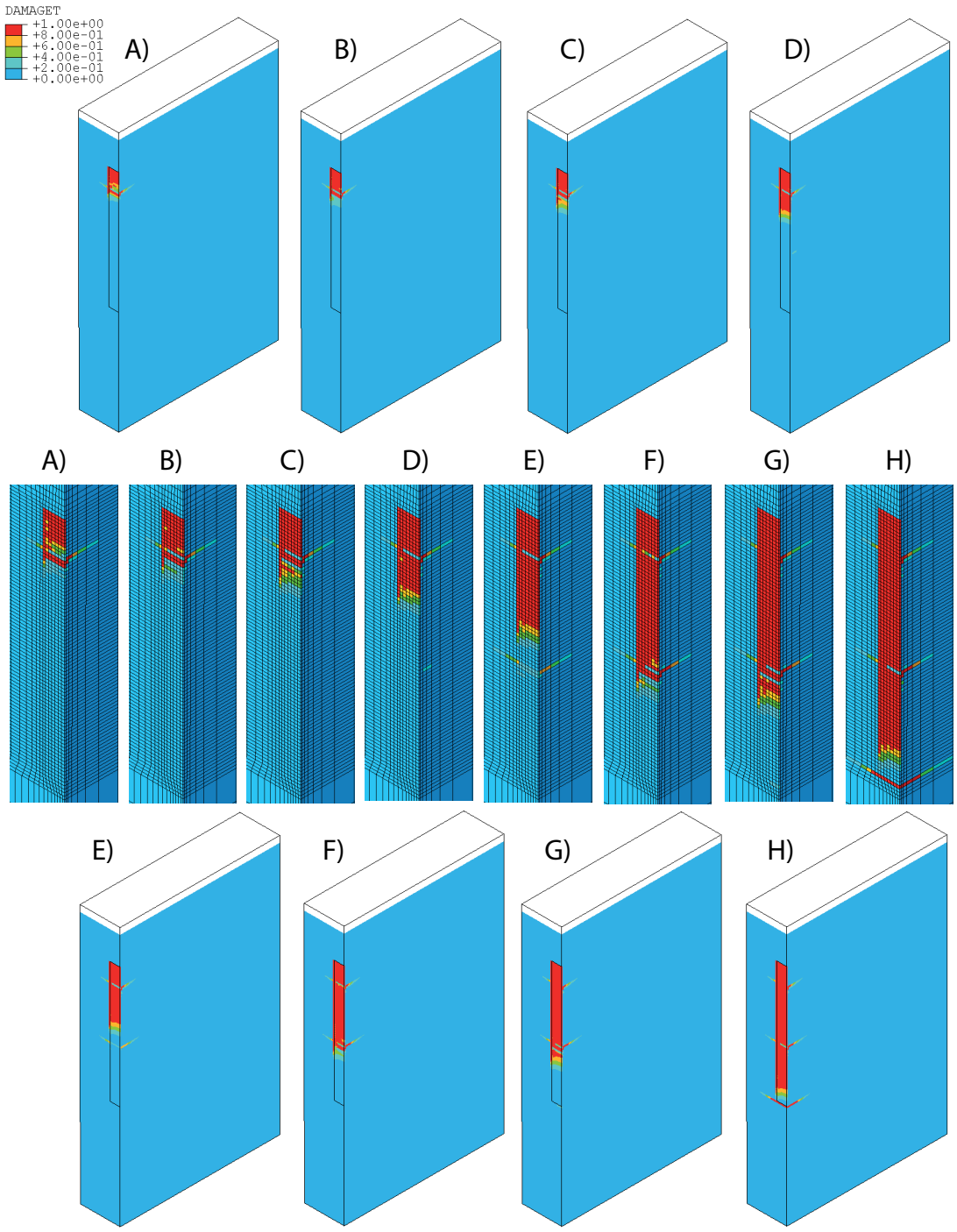

Figure 8: Tensile damage contour plots.

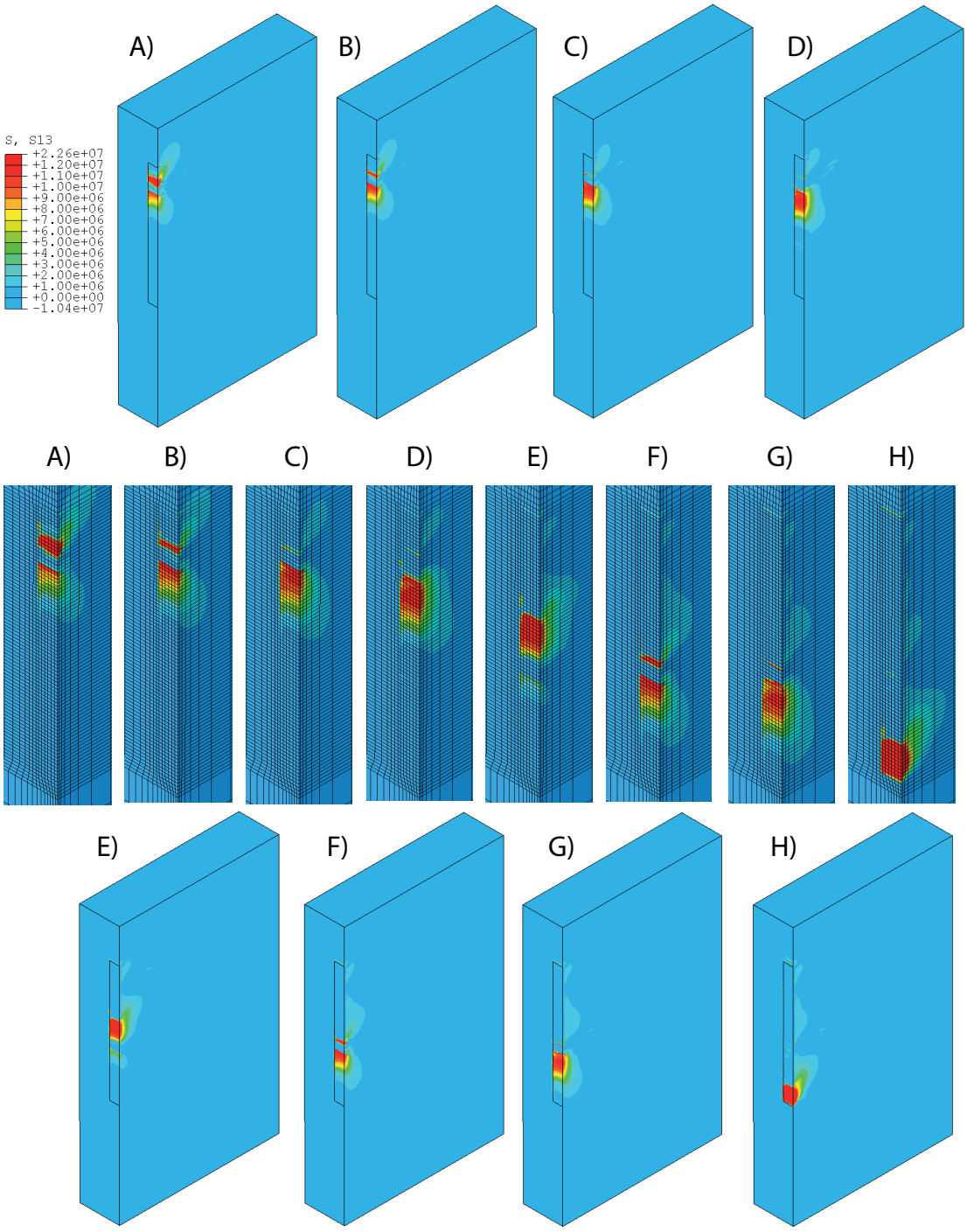

Figure 9: Shear stress contour plots.

5. Numerical investigation of open issues of the debonding phenomenon

The numerical model is used to investigate further the debonding process and gain a more comprehensive understanding of the debonding phenomenon, without the burden of performing additional tests that could be time-consuming and expensive. Indeed, the numerical model is also employed to evaluate: (i) the influence of geometrical and mechanical parameters, i.e. mortar joint thickness and mortar quality, and (ii) the effect of the FRP strip width on the single-lap test response.

Regarding the first task, Figures 10 and 11 collect the comparison in terms of applied load-global slip curves and longitudinal strain profiles, respectively, between the configuration presented in the previous section (labeled "Standard mortar joints") and the following arrangements, in which the dimensions of bricks have not been modified:

- the "Without mortar joints" arrangement, where the whole masonry specimen features the mechanical properties of brick;
- the "Standard joints-weak mortar" arrangement, where mortar has weaker mechanical properties with respect to the standard mortar joints case. In particular, a reduction factor equal to 2 for Young modulus and a reduction factor equal to 4 for compressive and tensile strengths have been assumed;
- the "Large joints-standard mortar" arrangement, where the thickness of mortar joints have been increased by a factor of 2 (from 8 to 16 mm) with respect to the "Standard mortar joint" case;
- the "Large joints-weak mortar" arrangement, where thicker mortar joints have been considered with the aforementioned reduced properties with respect to the "Standard mortar joint" case.

The comparison between the load response of the numerical simulation without the mortar joints and all the other simulations of Figure 10 suggests that the absence of mortar joints implies the absence of load drops. Additionally, load values of the simulation without mortar joints are grater than the others throughout the analysis. Therefore, it is clear that the area under such a curve is greater than the others, indicating a greater (although limited) energy supply throughout the debonding process with respect to the other arrangements.

By comparing the "Standard mortar joints" curve with the "Standard joints-weak mortar" one (Figure 10), it appears that they have a similar load path and they reach the same load values, although the arrangement with weak mortar generally presents greater values

of the global slip when compared with the "Standard mortar joints" scenario. Therefore, although weaker properties of the mortar do not alter the load at which the response levels off, a slightly greater deformability of the system is recorded due to the reduction (halved) of the stiffness of mortar.

The effect of larger joints on the applied load-global slip response implies greater load drops with respect to the "Standard mortar joints" case. Indeed, by comparing the "Standard mortar joints" curve with the "Large joints-standard mortar" one (Figure 10), it can be noted that in the larger joints case the two load drops are more pronounced and, even, the first peak load is substantially smaller than the first peak load in the "Standard mortar joints" case. However, after the first load drop, the value of the load at which the responses level off is approximately the same. Also in this case a slightly greater deformability of the structure is observed due to the increase (doubled) of the thickness of the mortar joints. The effect of weak mortar on large joints appears substantially the same as in the case of standard joints (Figure 10).

Figure 11 depicts the profiles of the strain component ε_{zz} along the center line of the bonded length for the different specimen arrangements. Overall, the strain profiles along the load response of the different arrangements are quite similar. However, some differences can be noted where the mortar joints are located. In particular, the magnitude of the strain component on the FRP where the mortar joints are located tends to be greater than the magnitude of the strain on the FRP surface corresponding to the adjacent bricks. This effect appears more pronounced when the mortar is weak, see Figure 11.

Figures 12-15 collect the geometry, an example of the shear stress transfer between the FRP strip and the masonry substrate when the stress transfer zone crosses the central mortar joint (at 57 mm $< z <$ 65 mm), and compressive and tensile damage distributions for the different arrangements described above. The shear stress contour plots are taken at the same global slip of point F (Figure 2). For the "Without mortar joints" arrangement (Figure 12), no interruption of the shear stress transfer occurs as mortar has the same properties of the brick. Furthermore, compressive and tensile damage distributions are limited to a single layer of finite elements. Conversely, the "Standard joints-weak mortar" specimen (Figure 13) shows a clear discontinuity of shear stress transfer where the mortar joint is located, which is similar to the case of "Standard mortar joints" arrangement (Figure 9). This discontinuity is observed also for the "Large joints-standard mortar" and "Large joints-weak mortar" specimens, in which the zone with almost-zero shear transfer is larger than the "Standard mortar joints" case, since the joints have the thickness doubled (Figures

14-15). This phenomenon appears to be responsible for more pronounced load drops, as shown in Figure 10. Additionally, in the case of weak mortar joints, the tensile damage distribution is wider and deeper along the joints than in standard mortar cases, due to the weaker properties of mortar. Deeper damage in mortar joints with weak mortar has been also observed in other experimental campaigns [43, 44]. As crack propagation deepens into the mortar joint, a different load response can be expected and load drops might be substituted by load bumps.

As can be noted in Figure 10, the analyses' responses in terms of force-slip curves are characterized by a slight increase of the load (if the drops are not considered) after the onset of debonding. The reason of this outcome is due to residual stresses in the brick and mortar constitutive laws (which have been adopted to guarantee convergence in the numerical analyses). Indeed, small amounts of shear stresses can be transferred in the zones where debonding occurred, see Figure 9. These shear stresses are generally one order of magnitude smaller than the ones transferred in the active debonding zone. However, they can lead to an overall slight increase of the load in the response rather than a plateau. This phenomenon can be assimilated to the outcomes in debonding experiments observed in inorganic-matrix composites where the presence of friction between the debonded component and the substrate determines an increase of the applied load after the onset of debonding. This could also be the case for FRP-substrate debonding, if the surface of the debonded region is not quite smooth. In the experimental campaign considered, the frictional effects were substantially negligible as the masonry block was able to rotate during the test while the strip was pulled vertically. This entail for the presence of a Mode-I condition, which reduced the frictional phenomena. However, the presence of residual stress in the constitutive law could be used roughly to represent frictional phenomena.

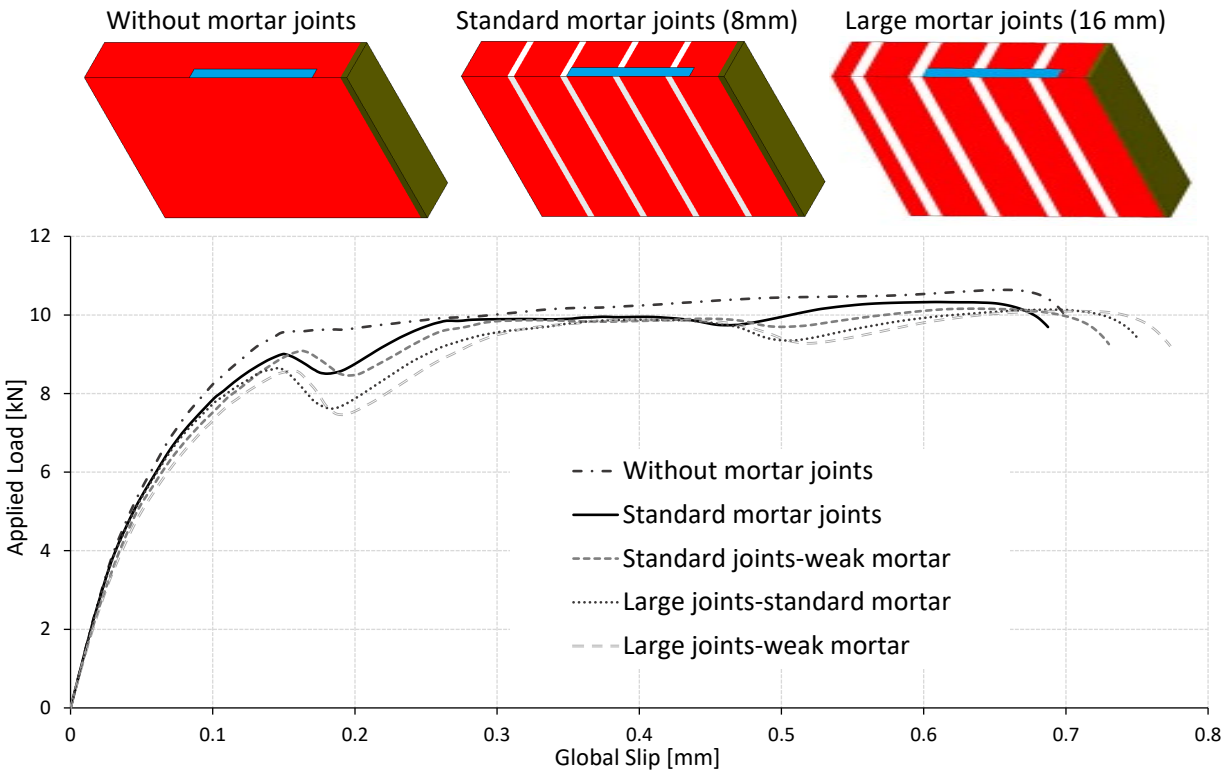

Figure 10: Comparison of applied load-global slip curves for different arrangements of the masonry specimen.

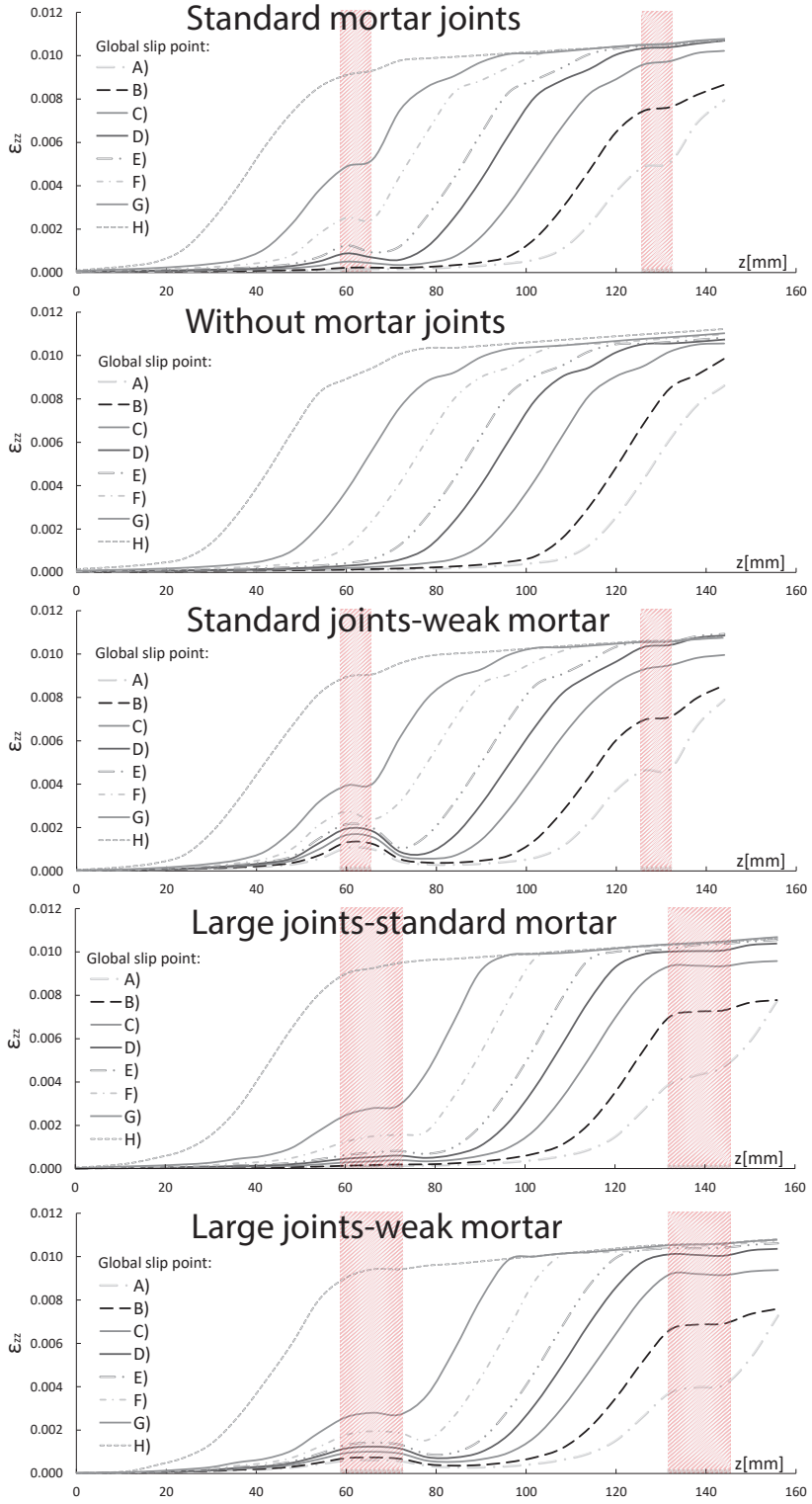

Figure 11: Comparison of longitudinal strain profiles for different specimen arrangements at given global slip points from Figure 2.

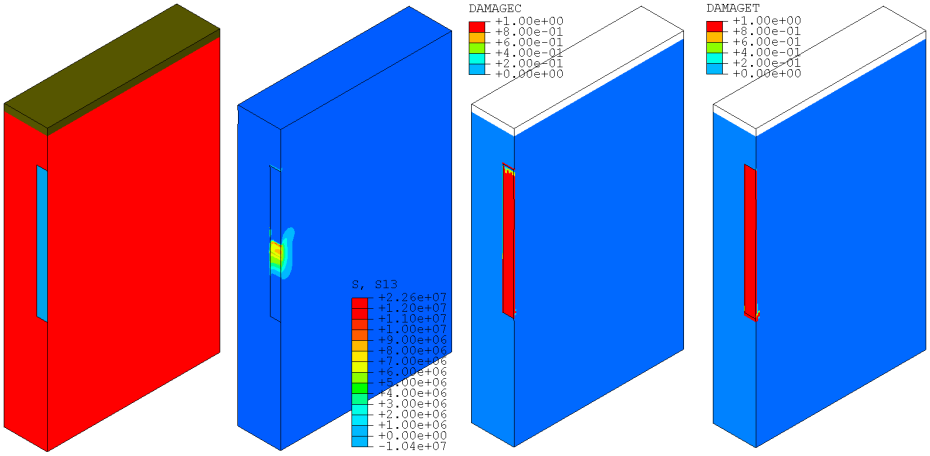

(a) (b) (c) (d)

Figure 12: "Without mortar joints" specimen contour plots: (a) configuration of the model, (b) example of shear stress transfer (Pa), (c) compressive and (d) tensile damage distributions at the end of the simulation.

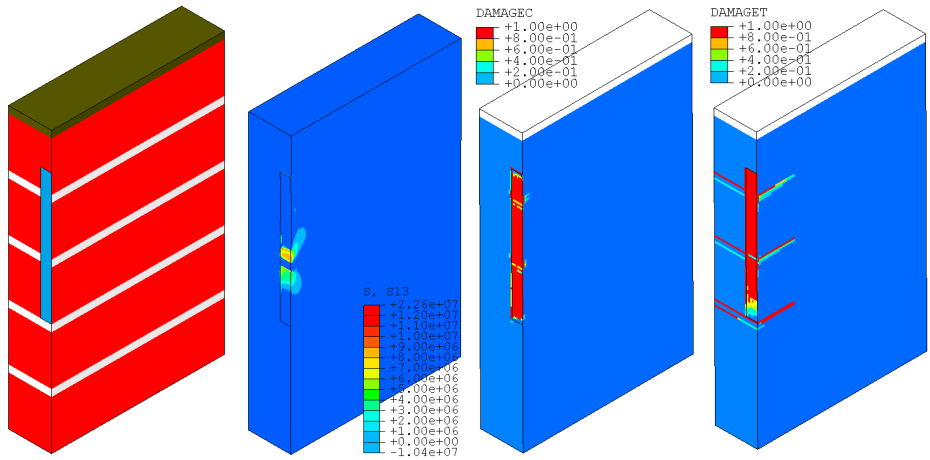

(a) (b) (c) (d)

Figure 13: "Standard joints-weak mortar" specimen contour plots: (a) configuration of the model, (b) example of shear stress transfer on a mortar joint (Pa), (c) compressive and (d) tensile damage distributions at the end of the simulation.

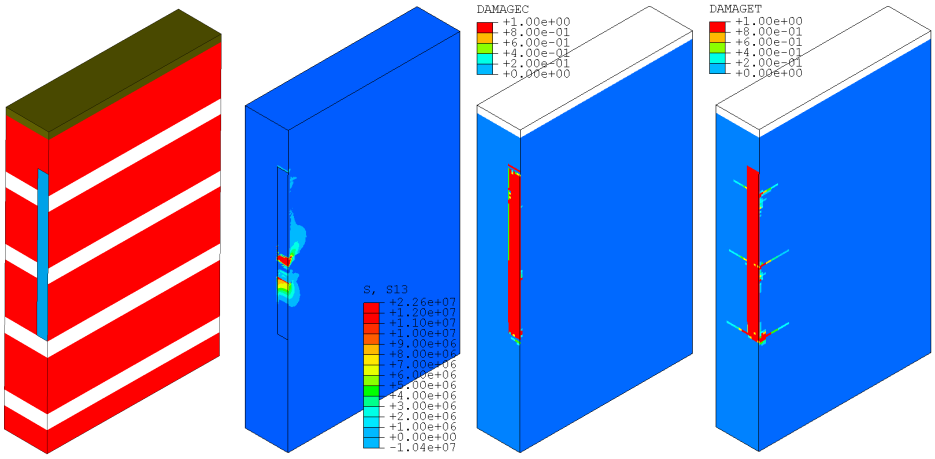

(a) (b) (c) (d)

Figure 14: "Large joints-standard mortar" specimen contour plots: (a) configuration of the model, (b) example of shear stress transfer on a mortar joint (Pa), (c) compressive and (d) tensile damage distributions at the end of the simulation.

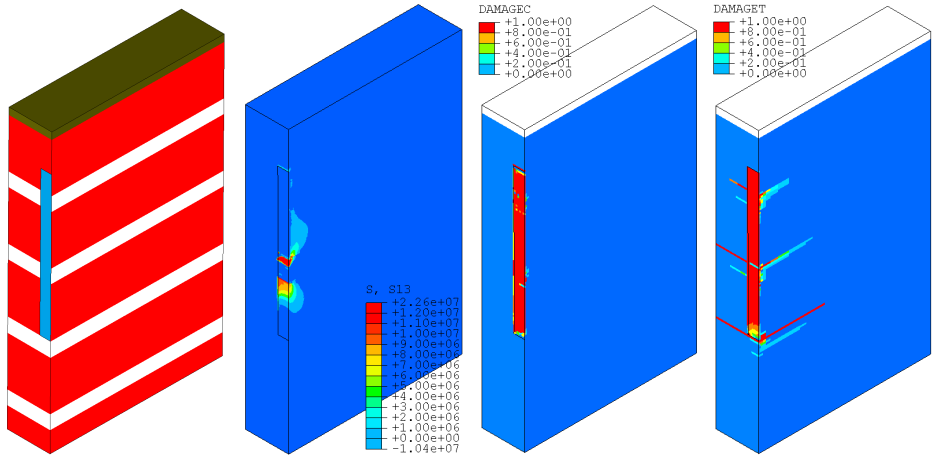

(a) (b) (c) (d)

Figure 15: "Large joints-weak mortar" specimen contour plots: (a) configuration of the model, (b) example of shear stress transfer on a mortar joint (Pa), (c) compressive and (d) tensile damage distributions at the end of the simulation.

Width effect investigation has been recently carried out on FRP-strengthened concrete [55, 56]. The numerical approach herein adopted is used to predict the width effect on load-carrying capacity of the FRP-masonry interface. To evaluate the effect of the width of the FRP strip on the single-lap shear test response, the numerical model is used to carry out a parametric study with several strip widths. Keeping the same masonry specimen and boundary conditions, five different FRP strip widths (b_f), collected in Figure 16 (top), are investigated and their results compared.

Figure 16 collects the numerical results in terms of applied load per unit width - global slip curves (middle) and peak loads per unit width (bottom) for the five b_f/b ratios, where b is the width of the masonry specimen (in this case $b = 100$mm). The peak load considered is the first peak load of the load-slip curve, as indicated in Figure 16 (middle) by a vertical dotted line. The peak loads per unit width show a variation of about 10% and by increasing the ratio b_f/b the value of peak load per unit width tends to a plateau, i.e. no significant variations of the peak load per unit width are observed for ratios $b_f/b \geq 0.3$. This aspect appears to be in good agreement with the width factor model recently proposed by Lin et al. [55] for FRP-to-concrete joints.

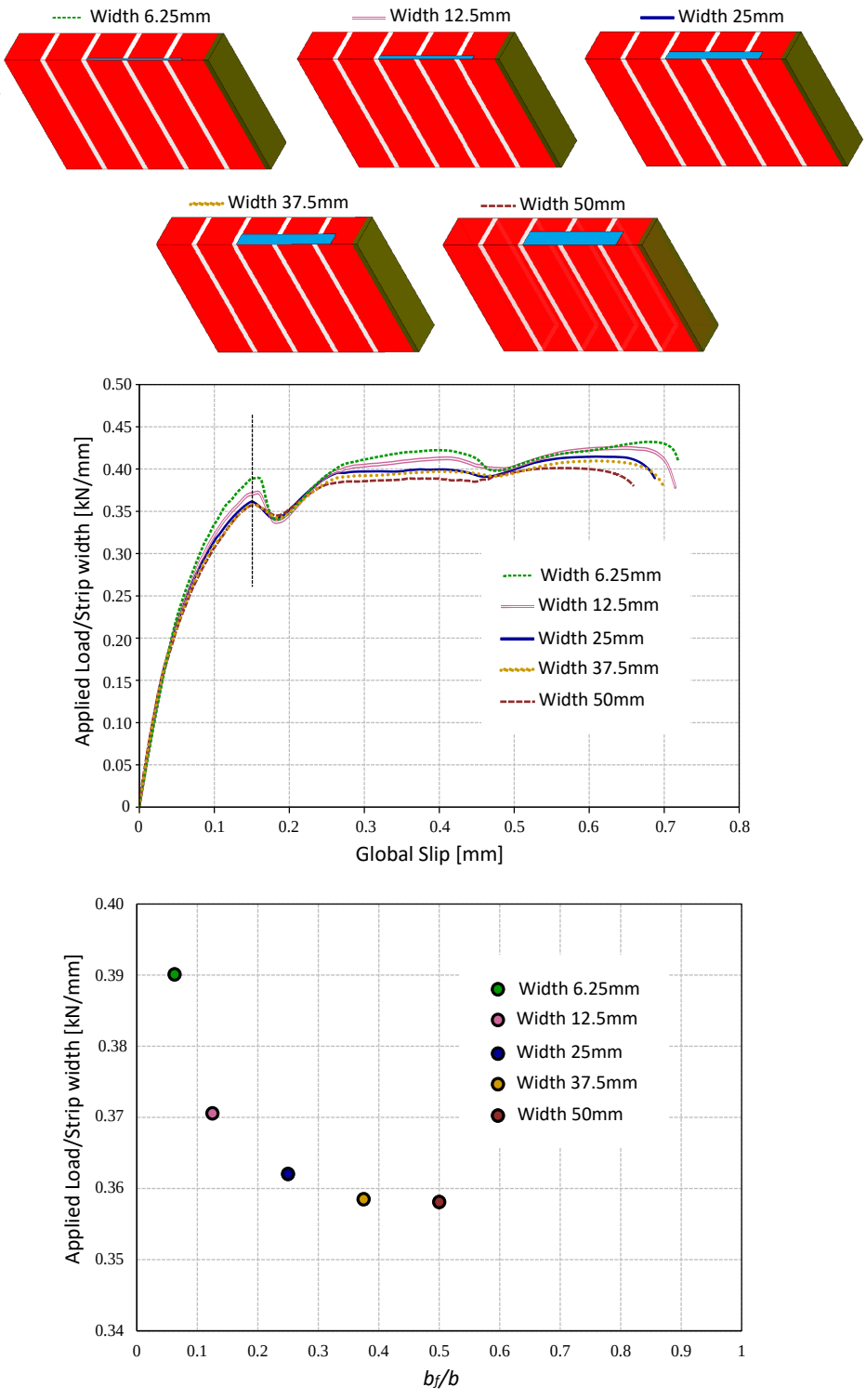

Figure 16: Width effect.

6. Conclusions

In this paper, the debonding phenomenon in FRP-strengthened masonry has been investigated by means of a numerical campaign. A 3D finite element model has been set up to simulate a single-lap shear test. Brick and mortar have been modeled separately by two plastic-damage constitutive laws and perfect adhesion between the FRP strip and masonry has been assumed.

Numerical results have been compared with experimental data. The periodic response of the transferable load at the FRP-masonry interface due to the effect of mortar joints has been confirmed by simulations. A good agreement between the experimental and numerical results has been observed.

Finally, further FE analyses have been carried out to gain an insight on the effects of the thickness and mechanical properties of mortar joints, and the width of the FRP strip on the debonding phenomenon. As a result, load drops have been directly related to the presence of mortar joints and larger load drops have been observed for thicker mortar joints. Furthermore, by increasing the FRP strip width, the peak load per unit width tends to a plateau, i.e. no significant variation of the peak load per unit width is observed when $b_f/b \geq 0.3$.

Acknowledgments

Financial support by the Italian Ministry of Education, Universities and Research MIUR is gratefully acknowledged (PRIN2015 "Advanced mechanical modeling of new materials and structures for the solution of 2020 Horizon challenges" prot. 2015JW9NJT_018).

References

[1] Ehsani MR, Saadatmanesh H, Al-Saidy A. Shear behavior of URM retrofitted with FRP overlays. Journal of Composites for Construction 1997;1(1):17-25.

[2] Triantafillou TC, Fardis MN. Strengthening of historic masonry structures with composite materials. Materials and Structures 1997;30:486-496.

[3] Luciano R, Sacco E. Damage of masonry panels reinforced by FRP sheets. International Journal of Solids and Structures 1998;35(15):1723-1741.

[4] Valluzzi MR, Tinazzi D, Modena C. Shear behavior of masonry panels strengthened by FRP laminates. Construction and Building Materials 2002; Special Issue, 16(7):409-416.

[5] Corradi M, Borri A, Vignoli A. Strengthening techniques tested on masonry structures struck by the Umbria-Marche earthquake of 1997-1998. Construction and Building Materials 2002;16 (4):229-239.

[6] Ascione L, Feo L, Fraternali F. Load carrying capacity of 2D FRP/strengthened masonry structures. Composites Part B 2005;36(8):619-626.

[7] Hamid AA, El-Dakhakhni WW, Hakam ZHR, Elgaaly M. Behavior of Composite Unreinforced Masonry - Fiber-Reinforced Polymer wall assemblages under In-Plane loading. Journal of Composites for Construction 2005;9(1):73-83.

[8] El-Gawady MA, Lestuzzi P, Badoux M. Aseismic retrofitting of unreinforced masonry walls using FRP. Composites Part B 2005;37(2):148-162.

[9] Shrive NG. The use of fibre reinforced polymers to improve seismic resistance of masonry. Construction and Building Materials 2006;20(4):269-277.

[10] Gilstrap JM, Dolan CW. Out-of-plane bending of FRP-reinforced masonry walls. Composites Science and Technology 1998;58(8):1277-1284.

[11] Hamoush S, McGinley M, Mlakar P, Scott D, Murray K. Out-of-plane strengthening of masonry walls with Reinforced Composites. Journal of Composites for Construction 2001;5(3):139-145.

[12] Kuzik MD, Elwi AE, Roger Cheng JJ. Cyclic flexure tests of masonry walls reinforced with Glass Fiber Reinforced Polymer sheets. Journal of Composites for Construction 2003;7(1):20-30.

[13] Mosallam AS. Out-of-plane flexural behavior of unreinforced red brick walls strengthened with FRP composites. Composites Part B 2007;38:559-574.

[14] Casareto M, Olivieri A, Romelli A, Lagomarsino S. Bond behavior of FRP laminates adhered to masonry. Proceedings International Conference Advancing with Composites (Plast), Milan, Italy; 2003.

[15] Aiello MA, Sciolti SM. Bond analysis of masonry structures strengthened with CFRP sheets. Construction and Buildings Materials 2006;20:90-100.

[16] Carloni C, Subramaniam KV. Investigation of the interface fracture during debonding between FRP and masonry. Advances in Structural Engineering 2009;12(5):731-743.

[17] Carloni C, Subramaniam KV. FRP/masonry debonding: numerical and experimental study of the role of mortar Joints. Journal of Composites for Construction 2012;16(5):581-589.

[18] Capozucca R. Experimental FRP/SRPhistoric masonry delamination. Composite Structures 2010;92:891-903.

[19] Grande E, Imbimbo M, Sacco E. Experimental and numerical investigations on the bond behavior of CFRP laminates glued on clay bricks. Composites Part B 2011;42(2):330-340.

[20] Kwiecien A. Stiff and flexible adhesives bonding CFRP to masonry substrates Investigated in pull-off test and Single-Lap test. Archives of Civil and Mechanical Engineering 2012;12:228-239.

[21] Mazzotti C, Ferracuti B, Bellini A. Experimental bond tests on masonry panels strengthened by FRP. Composites Part B 2015;80:223-237.

[22] Valluzzi MR, Oliveira DV, Caratelli A, Castori G, Corradi M, de Felice G, Garbin E, Garcia D, Garmendia L, Grande E, Iannirubertо U, Kwiecień A, Leone M, Lignola GP, Lourenço PB, Malena M, Micelli F, Panizza M, Papanicolaou CG, Prota A, Sacco E, Triantafillou TC, Viskovic A, Zając B, Zuccarino G. Round robin test for composite to brick shear bond characterization. Materials and Structures 2012;45:1761-1791.

[23] Capozucca R. Effect of mortar layers in the delamination of GFRP bonded to historic masonry. Composites Part B 2013;44:639-649.

[24] Carrara P, Ferretti D, Freddi F. Debonding behavior of ancient masonry elements strengthened with CFRP sheets. Composites Part B 2013;45(1):800-810.

[25] Ghiassi B, Xavier J, Oliveira DV, Lourenço PB. Application of digital image correlation in investigating the bond between FRP and masonry. Composite Structures 2013;106:340-349.

[26] Aiello MA, Sciolti MS. Analysis of bond performance between CFRP sheets and calcarenite ashlars under service and ultimate Conditions. Masonry International 2008;21(1):15-28.

[27] Faella C, Camorani G, Martinelli E, Paciello SO, Perri F. Bond behaviour of FRP strips glued on masonry: Experimental investigation and empirical formulation. Construction and Building Materials 2012;31:353-363.

[28] Ceroni F, Garofano A., Pecce M. Bond tests on tuff elements externally bonded with FRP materials. Materials and Structures 2015;48(7):2093-2110.

[29] Oliveira DV, Basilio I, Lourenço PB. Experimental bond behavior of FRP sheets glued on brick masonry. Journal of Composites for Construction 2011;15(1):32-41.

[30] Fagone M, Ranocchiai G, Briccoli Bati S. An experimental analysis about the effects of mortar joints on the efficiency of anchored CFRP-to-masonry reinforcements. Composites Part B 2015;76:133-148.

[31] de Felice G, Aiello MA, Bellini A, Ceroni F, De Santis S, Garbin E, Leone M, Lignola GP, Malena M, Mazzotti C, Panizza M, Valluzzi MR. Experimental characterization of composite-to-brick masonry shear bond. Materials and Structures 2015. Doi: 10.1617/s11527-015-0669-4.

[32] Ceroni F, de Felice G, Grande E, Malena M, Mazzotti C, Murgo F, Sacco E, Valluzzi MR. Analytical and Numerical modeling of composite-to-brick bond. Materials and Structures 2014;47:1987-2003.

[33] Focacci F, Carloni C. Periodic variation of the transferable load at the FRP-masonry interface. Composite Structures 2015;129:90-100.

[34] Carloni C, Focacci F. FRP-masonry interfacial debonding: An energy balance approach to determine the influence of the mortar joints. European Journal of Mechanics A/Solids 2016;55:122-133.

[35] Freddi F, Sacco E. Mortar joints influence in debonding of masonry element strengthened with FRP. Key Engineering Materials 2015;624:197-204.

[36] Freddi F, Sacco E. An interphase model for the analysis of the masonry-FRP bond. Composite Structures 2016, 138, 322334. doi:10.1016/j.compstruct.2015.11.041

[37] Mazzotti C, Murgo FS. Numerical modelling and experimental verification of GFRP-masonry interface behaviour: bond evolution and role of the mortar layers. Composites Part B 2014;75:212-225.

[38] Fedele R, Milani G. Assessment of bonding stresses between FRP sheets and masonry pillars during delamination tests. Composites Part B 2012;43:1999-2011.

[39] Fedele R, Milani G. A numerical insight into the response of masonry reinforced by FRP strips. The case of perfect adhesion. Composite Structures 2010;92(10):2345-2357.

[40] Fedele R, Milani G. Three-dimensional effects induced by FRP-from-masonry delamination. Composite Structures 2011;93(7):1819-1831.

[41] Ghiassi B, Oliveira DV, Lourenço PB, Marcari G. Numerical study of the role of mortar joints in the bond behavior of FRP-strengthened masonry. Composites Part B 2013;46:21-30.

[42] Mazzotti C, Savoia M, Ferracuti B. A new single-shear set-up for stable debonding of FRPconcrete joints. Construction and Building Materials 2009;23(4):1529-1537.

[43] Ceroni F, Leone M, Rizzo V, Bellini A, Mazzotti C. Influence of mortar joints on the behaviour of

FRP materials bonded to different masonry substrates. Engineering Structures 2017;153:550-568.
[44] Sassoni E, Sarti V, Bellini A, Mazzotti C, Franzoni E. The role of mortar joints in FRP debonding from masonry. Composites Part B: Engineering 2018;135:166-174.
[45] Lee J, Fenves GL. Plastic-Damage Model for Cyclic Loading of Concrete Structures. Journal of Engineering Mechanics 1998;124(8):892-900. doi:10.1061/(asce)0733-9399(1998)124:8(892)
[46] Abaqus®. Theory manual, version 6.14; 2014.
[47] Milani G, Valente M, Alessandri, C. The narthex of the Church of the Nativity in Bethlehem: A non-linear finite element approach to predict the structural damage. Computers & Structures 2017. doi:10.1016/j.compstruc.2017.03.010
[48] van der Pluijm. Shear Behaviour of bed joints. In: Abrams DP, editor. Proceedings of 6th North American masonry conference, Philadelphia, USA, 6-9 June, 1993,125-136.
[49] D'Altri AM, Castellazzi G, de Miranda S, Tralli A. . Seismic-induced damage in historical masonry vaults: A case-study in the 2012 Emilia earthquake-stricken area. Journal of Building Engineering 2013;13:224243. doi:10.1016/j.jobe.2017.08.005
[50] Castellazzi G, D'Altri AM, de Miranda S, Chiozzi A, Tralli, A. Numerical insights on the seismic behavior of a non-isolated historical masonry tower. Bulletin of Earthquake Engineering 2017. doi:10.1007/s10518-017-0231-6
[51] Lubliner J, Oliver J, Oller S, Oñate E. A plastic-damage model for concrete. International Journal of Solids and Structures 1989;25(3):299-326. doi:10.1016/0020-7683(89)90050-4
[52] Castellazzi G, D'Altri AM, de Miranda S, Ubertini F. An innovative numerical modeling strategy for the structural analysis of historical monumental buildings. Engineering Structures 2017;132:229-248. doi:10.1016/j.engstruct.2016.11.032
[53] Kaushik HB, Rai DC, Jain SK. Stress-Strain Characteristics of Clay Brick Masonry under Uniaxial Compression. Journal of Materials in Civil Engineering 2007;19(9):728-739. doi:10.1061/(asce)0899-1561(2007)19:9(728)
[54] Ceroni F, Ferracuti B, Pecce M, Savoia M. Assessment of a bond strength model for FRP reinforcement externally bonded over masonry blocks. Composites Part B: Engineering 2014;61:14761. doi.org/10.1016/j.compositesb.2014.01.028
[55] Lin JP, Wu YF, Smith ST. Width factor for externally bonded FRP-to-concrete joints. Construction and Building Materials 2017, 155, 818829. doi:10.1016/j.conbuildmat.2017.08.104
[56] Xu T, He ZJ, Tang CA, Zhu WC, Ranjith PG. . Finite element analysis of width effect in interface debonding of FRP plate bonded to concrete. Finite Elements in Analysis and Design 2015;93:3041. doi:10.1016/j.finel.2014.08.009